Eur. Phys. J. B **47**, 495–501 (2005)
DOI: 10.1140/epjb/e2005-00351-8

THE EUROPEAN PHYSICAL JOURNAL B

Spectral cut-off in the efficiency of the resistive state formation caused by absorption of a single-photon in current-carrying superconducting nano-strips

A. Semenov[1,a], A. Engel[1,2], H.-W. Hübers[1], K. Il'in[3], and M. Siegel[3]

[1] DLR Institute of Planetary Research, Rutherfordstr. 2, 12489 Berlin, Germany
[2] Physics Institute, University of Zurich, Winterthurerstrasse 190, 8057 Zurich, Switzerland
[3] Institute of Micro- and Nano-Electronic Systems, University of Karlsruhe, Hertzstr. 16, 76187 Karlsruhe, Germany

Received 25 September 2004 / Received in final form 18 August 2005
Published online 17 November 2005 –

Abstract. We have studied supercurrent-assisted formation of the resistive state in nano-structured disordered superconducting Nb(N) films after absorption of a single optical to near-infrared photon. The efficiency of the resistive state formation has a pronounced spectral cut-off; corresponding threshold photon energy decreases with the bias current. Analysis of the experimental data in the framework of the refined hot-spot model suggests that the quantum yield for near-infrared photons increases with the photon energy. Relaxation of the resistive state depends on the photon energy making the phenomena feasible for the development of energy resolving single-photon detectors.

PACS. 74.78.-w Superconducting films and low-dimensional structures – 42.50.Nn Quantum optical phenomena in absorbing, dispersive and conducting media – 74.40.+k Fluctuations (noise, chaos, nonequilibrium superconductivity, localization, etc.)

1 Introduction

A recently proposed hot-spot scenario of the resistive state formation in a thin, narrow, current-carrying superconducting strip due to absorption of a single infrared photon [1] was subsequently suggested as the mechanism of single-photon detection [2,3] in epitaxial NbN microbridges. It was shown that the detection efficiency increases exponentially with both the current and the photon energy. Knee-like features in the overall exponential dependence of the quantum efficiency on the bias current were attributed [3] to the spectral cut-off of the detection efficiency predicted by the hot-spot model. The dynamic suppression of the energy gap by the bias current has been proven [4] to cause a delay of the resistive state formation with respect to the photon arrival in NbN meander lines. However, the quantitative evaluation of the delay time as well as the knee-like features in the quantum efficiency implied the normal-spot size much larger than the hot-spot model [5] predicts.

A thorough theoretical description of the experimental situation would require to solve the Time Dependent Chang-Scalapino (TDCS) or Ginsburg-Landau (TDGL) equations supplemented by the diffusion of quasiparticles and their generation by the current. The TDGL approach made it possible to explain the time delay in the formation of the resistive state [4] and the magnitude of the voltage noise [6] of the single-photon detectors. On the other hand, analysis of a joint solution of the TDCS and diffusion equations [7] suggested that the spatial dynamics of the non-equilibrium quasiparticles in a detector can be well described by diffusion only if the diffusion of quasiparticles across the device takes much more time than their avalanche-like multiplication after absorption of an infrared photon. This approach was implemented for modelling Nb and NbN hot-electron mixers [8,9] an also in the hot-spot model [1,5] of single-photon detectors. The hot-spot model describes the formation and evolution of a normal spot in an infinite homogeneous superconducting film around the site where a single photon has been absorbed. Accordingly, the resistive state in a narrow current-carrying superconductor appears when the normal spot becomes large enough allowing the current to locally destroy superconductivity. Experimental consequences of the hot-spot scenario are fairly independent on the particular mechanism, which controls breaking down the superconducting state. It can be formation of a phase slip center, uniform suppression of the energy gap or nucleation of magnetic vortices. The number of photons, which result in a temporary existing resistive state, related to the number of photons crossing the geometrical area of the superconductor presents the quantum efficiency of the

[a] e-mail: alexei.semenov@dlr.de

resistive state formation. Since the size of the normal spot increases with the photon energy, the hot-spot model suggests a long-wavelength cut-off in the quantum efficiency. Although the spectral cut-off is a universal feature of any hot-spot model it has not been undoubtedly observed so far, instead an almost monotonous decrease of the quantum efficiency with the photon wavelength has been found.

In this work we report measurements of the quantum efficiency of the resistive state formation in disordered Nb(N) films, which demonstrate predicted cut-off. We refine the hot-spot model taking into account non-equilibrium quasiparticles outside the normal spot and show that the formation of the resistive state in the absence of fluctuation may be triggered by a single photon even though no normal spot appears. We also present recent results showing that the resistive state created by a photon "remembers" its energy, i.e. the effect has energy resolving capability.

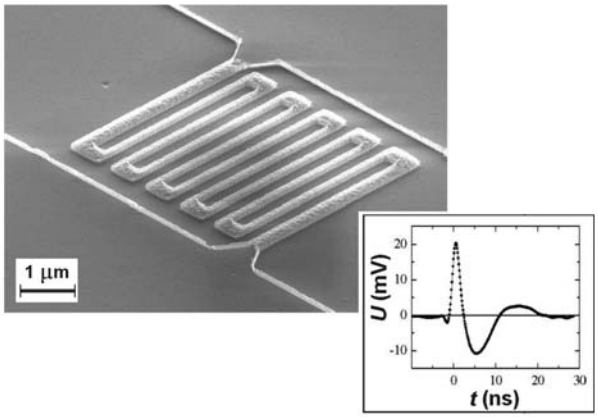

Fig. 1. Photo of the representative Nb meander on Si substrate made with a scanning electron microscope. Visible fringes at the edges of the structure are formed by photolack left for device protection. Inset shows a typical voltage pulse recorded by the oscilloscope.

2 Experiment

2.1 Sample characterisation and measurement technique

Experimental results were obtained with narrow meander lines made from either Nb or Nb(N) thin films. The meander covering an area of 4×4 μm^2 was used in order to increase optical coupling with near infrared photons. Contrary to the conventional polycrystalline NbN films with the B1 structure, our disordered Nb(N) films were prepared by dc magnetron sputtering of an Nb target in an Ar+N_2 gas admixture that had a reduced partial pressure of N_2. Films with a nominal thickness of 5 nm were deposited on sapphire substrates kept at room temperature. The deposition regime in combination with relatively high sputtering rates of about 1.2 nm/s resulted in disordered films with a nitrogen content smaller than in stoichiometric composition. Mostly because of the nitrogen deficiency, the superconducting transition in 5 nm thick films occurred at ≈6 K that is about one third of the transition temperature of bulk stoichiometric NbN. Moreover, the transition temperature was partly suppressed due to the proximity effect [10] between the central superconducting part of the film and its non-superconducting oxidized surface on one side and film-substrate interlayer on the other side. Films were patterned using electron-beam lithography and ion milling. Our Nb films had a thickness of 10 nm and were deposited on Si substrates by dc magnetron sputtering in pure Ar atmosphere and patterned using electron-beam lithography and reactive ion etching. The line width was 84 nm and 98 nm and the normal state resistivity just above the superconducting transition was 6×10^{-6} Ω cm and 6.7×10^{-4} Ω cm for Nb and NbN meanders, respectively. Due to a partial damage of strip edges by argon ions during the etching process, a portion of the meander line near the edges became normal. These normal areas further decreased [11] the transition temperature. For both materials the transition temperature T_C of the meanders varied between 4 and 5 K. Study performed with a scanning electron microscope suggested that the geometric non-uniformity of the line-width in our meanders was less than 15%. An image of the representative Nb meander on the Si substrate is shown in Figure 1.

We evaluated parameters of our NbN structures relevant to the formation of the resistive sate. Measuring the temperature variations of the second critical magnetic field B_{c2} near T_C, we concluded the diffusion coefficient $D = 0.35$ cm^2 s^{-1}. This relatively low electron diffusivity assures that the meanders are in the diffusive, dirty limit. Extrapolating the linear temperature dependence of B_{c2} near T_C, we found $B_{c2}(0) = 9.4$ T and the zero-temperature coherence length $\xi_0 = (\Phi_0/\pi B_{c2}(0))^{1/2} \approx 8.5$ nm. The density of electronic states $N_0 = 2.2 \times 10^{24}$ m^{-3} K^{-1} is then deduced from the Einstein's relation $N_0 = 1/(e^2\ \rho\ D)$ where ρ is the normal-state resistivity. Further assuming a classical energy gap $\Delta_0 = 1.76\, k_B\, T_C$, we estimated the London penetration depth $\lambda_L(0) = 1200$ nm. We also measured the critical current density in our meander lines as a function of temperature. Because the width of the meander is well below the London penetration depth, the supercurrent density is uniform across the cross-section. To derive the critical current density from the measured values of the critical current we rather used the electrical cross-section of the meander. Due to the proximity effect at the lateral interfaces and the damaged strip edges it was almost one half [11] of the geometrical cross-section $d\,w$, where d and w are the thickness and the width of the meander, respectively. The best fit of the measured temperature dependence with the theoretical mean-field temperature dependence $j(T) = 3.27 e N_0 \Delta_0 (k_B T_C D/h)^{1/2}(1 - (T/T_C)^2)(1 - (T/T_C)^4)^{1/2}$ resulted in $N_0 = 2.7 \times 10^{24}$ m^{-3} K^{-1} in agreement with the density of states inferred from the film resistivity. Practical coincidence of the measured critical current with the depairing current confirms that our films are strongly disordered and have a large concentration of defects acting as pinning

centers. A granular structure, which is typical for relatively thick slowly grown NbN films, may not appear in our films because of the high deposition rate [12]. However, if any intergranular barriers are present in our films, they do not reduce the density of the critical current and should not therefore effect diffusion of electrons.

We shall now estimate the quasiparticle thermalization time τ_{th} and the electron-phonon interaction time τ_{ep} in our films, which are both important for understanding the dynamics of a hot-spot. Almost the same thermalization time of ≈7 ps was computed for Nb [7] and experimentally measured for conventional B1 NbN films [13]. Taking into account typical for disordered dirty metals linear dependence of the reciprocal thermalization time on the energy, we estimate for our films with reduced energy gap $\tau_{th} \approx 14$ ps. There is not much information available on the electron-phonon interaction time in disordered nitrogen deficient NbN films. However, it is unlikely that τ_{ep} in those films appears much shorter than the electron-phonon interaction time in conventional B1 films. We therefore accept the value of τ_{ep} in B1 films as the lower boundary for the electron-phonon interaction time in our films, that is $\tau_{ep}(4\ \mathrm{K}) > 60$ ps.

The substrate carrying the meander was thermally anchored to the cold plate of a He^4–bath cryostat and was operated at temperatures ranging from 1.8 to 3.0 K. The meander was illuminated using an incandescent light source. To enable spectral measurements, the light was passed through a prism monochromator. The meander was voltage-biased through a voltage divider mounted inside the cryostat. Estimated time constant of the bias was 0.5 ns. The response to illumination was in the form of a random sequence of voltage transients. Each of them revealed temporary existing resistive state due to either a dark count event or absorption of a photon. Transients were amplified using broadband microwave amplifiers (noise temperature 6 K, band-pass from 0.1 GHz to 1.6 GHz) and then guided either to a 250 MHz bandwidth/1 GHz sampling rate oscilloscope or to a 200 MHz bandwidth voltage-level counter. Inset in Figure 1 shows the resulting signal recorded by the oscilloscope. The mean photon count rate, that is proportional to the quantum efficiency, was normalized to the light intensity measured with either a silicon photodiode or a PbSe photodiode (at longer wavelengths). For dark count measurements the optical entrance of the cryostat was blocked completely. Varying the discriminator level of the counter, we measured the integral of the statistical distribution of the transient amplitude and retrieved the mean value and the dispersion.

2.2 Experimental data

The normalized quantum efficiency for Nb and NbN meanders are compared in Figure 2. For both materials it was measured at 1.8 K with the current $I = 0.9\,I_C$ where I_C is the critical current at the operation temperature. The quantum efficiency for the Nb meander drops continuously with the increase of the wavelength showing no threshold

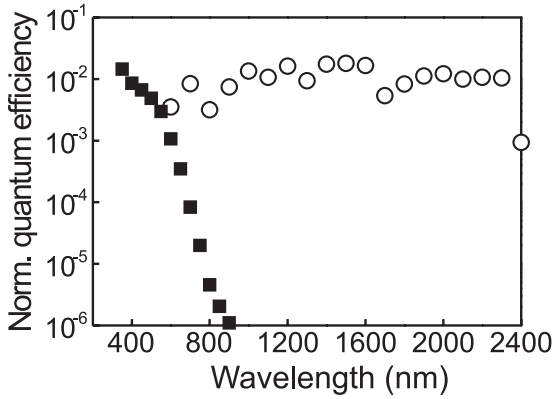

Fig. 2. Normalized quantum efficiency for Nb (closed symbols) and NbN (open symbols) meanders.

features while the NbN meander demonstrates an almost constant efficiency of ≈1% up to a wavelength that exceeds 2 μm. Obviously, the spectral cut-off for both specimens falls out of our experimental range. For Nb it may occur at a wavelength less than 0.25 mm while for NbN the corresponding threshold wavelength exceeds 2.3 mm. According to the model described in the next section, the threshold wavelength should be proportional to $\rho\, D^{1/2} \Delta_0^{-2}\, d^{-1}$. Given the difference in the resistivity, the film thickness and the electron diffusivity, more than an order of magnitude difference between the threshold wavelength for Nb and NbN meanders is easily understood. In the sections that follow we concentrate exclusively on NbN.

A decrease of the current brings to light the cut-off of the quantum efficiency in the NbN meanders. This can be seen in Figure 3 that shows relative quantum efficiency of a representative NbN meander at 2 K for different bias currents. For each current there is a plateau in the wavelength dependence of the quantum efficiency that is followed by the drop as the wavelength increases. The constant and falling portions are approximated by the straight lines. The threshold values of the wavelength are marked by arrows. They are defined as the wavelengths corresponding to the intersections of the approximating lines.

Alternatively, varying the current through a meander exposed to illumination at a fixed wavelength, we also observed the cut-off in the photon count rate. Figure 4 shows the current dependence of the photon count rate for different photon energies and the current dependence of the dark count rate. Indeed, when the bias current is close to the critical value, all data points representing photon count rate merge and the count rate slowly varies with the current. The points corresponding to the particular wavelength start to deviate from this common dependence at a current that increases with the wavelength. We associate the deviation from the common dependence with the cut-off of the quantum efficiency. Values of the threshold bias current (I^*) were obtained from the best fit (shown by solid lines) of the photon count rate beyond the cut-off by the current dependence (dotted line) of the dark count rate. To obtain the fit, the I/I_C values in the current dependence of the dark count rates were multiplied by $I_C/I_C^<$

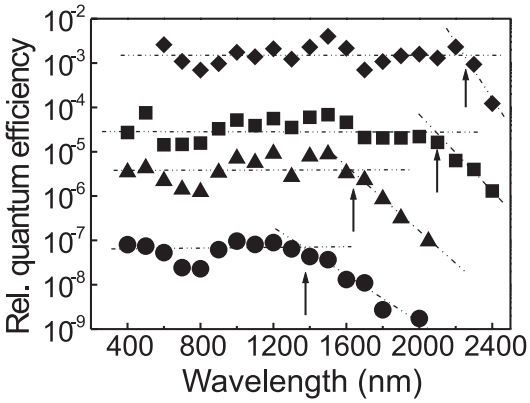

Fig. 3. Relative quantum efficiency for a representative NbN meander biased with currents $0.6\,I_C$, $0.77\,I_C$, $0.8\,I_C$ and $0.89\,I_C$ (from bottom to top). For convenience, the data sets are shifted arbitrarily along the vertical axis. Straight lines show least square linear approximations of the efficiency above and beyond the spectral cut-off. Arrows mark intersections of the approximating lines. Corresponding wavelengths are interpreted as the threshold values.

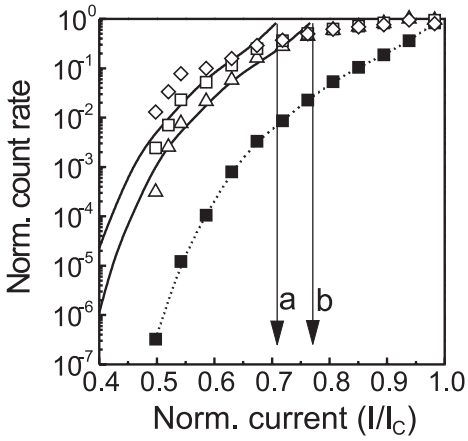

Fig. 4. Photon count rate (open symbols) for wavelengths 0.8 μm (diamonds), 1.4 μm (squares) and 2 μm (triangles) and dark count rate (closed squares) both normalized to the maximum observed count rate 5×10^7 s^{-1}. The data were acquired at 0.5 T_C. The dotted line is the least square polynomial fit of the dark count rate. Solid lines show the best fit of the photon count rate beyond the cut-off. Arrows mark the threshold value of the normalized current corresponding to the cut-off at 1.4 μm (a) and 2 μm (b).

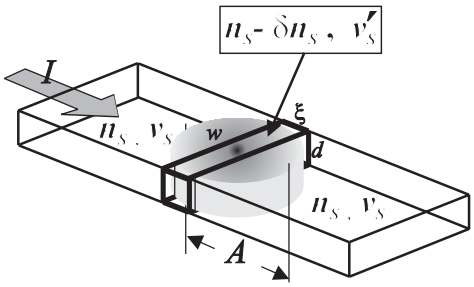

Fig. 5. Schematics of the superconducting strip-line carrying a current I. Bold lines demarcate the smallest volume where a reduction of the number of superconducting electron pairs causes the change of their mean velocity. Grey cylinder depicts the cloud of nonequilibrium quasiparticles with the size A.

where $I_C^< < I_C$ is the reduced critical current associated with the photon absorption site. The reduced critical current was the only fitting parameter. The best fit values of the ratio I^*/I_C are marked by arrows; they correspond to the intersection of the fitting curves and the level of the highest count rate. To justify this approach we point out that in a homogeneous meander a photon counting event beyond the cut-off may only appear as a fluctuation assisted event, i.e. a dark count associated with the portion of the detector where the critical current has temporarily reduced after photon absorption.

A slow increase of the photon count rate above the cut-off is related to the always present fluctuation assisted events. Current destroys the symmetry of the pair energy states in a superconductor making the excitation energy for some of electron pairs smaller than the energy gap at zero-current. Although well below T_C the mean excitation energy (the energy gap) does not vary much with the current [14], the probability of fluctuations assisted photon counts increases. We believe that these fluctuation assisted photon counts cause the weak current dependence of the measured full photon count rate above the cut-off.

3 Model refinement

Applying to our experimental data (Figs. 3, 4) the cut-off criteria [5] of the hot-spot model for the size of the normal spot $A_n = (1 - I^*/I_C)\,w$, we find the spot size of 8.5 nm created by the photon with a wavelength of 1.2 mm. An analytical approximation [5] of the numerical solution of the two dimensional diffusion problem gives a close value of ≈9 nm. According to the hot-spot model, even smaller normal spot should appear in conventional NbN films with B1 structure because they have a larger density of states, a larger energy gap and a larger electron diffusivity. Thus estimated sizes of the normal spot are all comparable or less than the coherence length suggesting that no resistive state should appear in response to photons with larger wavelength. Contrary, our experimental data show that not only the resistive state appear but there is a pronounced spectral cut-off corresponding to wavelengths larger than 1.2 μm. In order to eliminate this discrepancy, we will refine the hot-spot-model considering non-equilibrium quasiparticles, which are not confined in the normal spot [15].

Let a strip-line made of a superconducting film carry a supercurrent as it is shown in Figure 5. The film thickness is chosen smaller than both the line width and the coherence length ξ assuring the applicability of a two-dimensional diffusion model for nonequilibrium electrons. The small film thickness results in a large magnetic penetration length that exceeds the line width even at temperatures well below the superconducting transition temperature. In this geometry the local velocity of paired

electrons remains constant through the cross-section of the line. The local supercurrent density $j = e\,n_s v_s$ is associated with the velocity v_s and the local density n_s of paired electrons. Without magnetic perturbations the local current state may noticeably change only if n_s changes over a distance ξ or larger along the current path, shorter disturbances are tunnelled by electron pairs without energy dissipation. The smallest volume of the strip relevant to a current change, the ξ-slab, is marked in Figure 5 with bold lines. If the mean value of n_s in the ξ -slab decreases by an amount δn_s, the mean pair velocity increases and becomes

$$v_s' = \frac{n_s}{n_s - \delta n_s}\, v_s \qquad (1)$$

as required by the charge flow conservation. The characteristic conversion time of the pair velocity practically equals the Ginzburg-Landau relaxation time $\approx h/\Delta$ (Δ is the temperature dependent energy gap) and is small compared to the electron thermalization time τ_{th}. Thus, the pair velocity in the slab instantaneously follows changes of the mean pair density. The ξ-slab switches in the normal state if the pair velocity exceeds the critical value v_{sc} that corresponds to the critical current density $j_C = e\,n_s v_{sc}$ in the absence of excitations. This refined picture of the critical state suggests that no normal spot is required for the resistive state to temporary appear.

The concentration of nonequilibrium electrons $C(r,t)$ at the distance r from the photon absorption site evolves in time t due to multiplication of electrons and their diffusion out of the absorption site

$$C(r,t) = \frac{M(t)}{4\,\pi D\,d\,t}\ \exp\left(-\frac{r^2}{4\,D\,t}\right), \qquad (2)$$

where $M(t)$ describes the evolution of the full number of nonequilibrium electrons in time. At $\tau_{ep} \geq t \geq \tau_{th}$ nonequilibrium electrons have thermalized to the energy level Δ effectively becoming quasiparticles (QP). Their number reaches the maximum value $M(\tau_{th}) = \zeta\,\epsilon/\Delta$ where $\zeta \leq 1$ is the efficiency of the QP multiplication. After the thermalization time τ_{th} has elapsed and before subgap phonons appear, the concentration of nonequilibrium quasiparticles locally equals the reduction of superconducting electrons δn_s. Assuming that well below the transition temperature $n_s \approx N_0\Delta$, one can rewrite equation (1) and find the smallest number of nonequilibrium QP that is sufficient for switching the ξ-slab into the normal state

$$\delta N^* = N_0 \Delta\,\xi\,w\,d\,(1 - I/I_C). \qquad (3)$$

If the spread of the QP cloud is comparable to the coherence length, all quasiparticles contribute to the change of the pair velocity and $\delta n_s = M(\tau_{th})/(w\,d\,\xi)$. If the cloud is larger (see Fig. 5), only the part of quasiparticles confined within the ξ-slab has to be taken into account. The size $A(t)$ of the electron cloud is twice the radius of the spot that confines all nonequilibrium electrons. Equating $M(t)$ to the integral of the electron concentration (Eq. (2)) over the cylinder with the radius $A(t)/2$ and the thickness d, we find the time dependent size of the electron cloud $A(t) = 4[D\,t\,\ln(M(t))]^{1/2}$. If $M(\tau_{th}) \geq 100$ and the parameters of our films are considered, $A(t)$ exceeds the coherence length already at an early thermalization stage $t < \tau_{th}$. For $A \gg \xi$ the absolute number δN of nonequilibrium electrons confined to the ξ-slab can be evaluated analytically. Integrating electron concentration (Eq. (2)) over the slab results in $\delta N = M(t)\,\xi\,/(\pi\,D\,t)^{1/2}$. The number of nonequilibrium electrons in the slab peaks at $t \approx \tau_{th}$ when nonequilibrium electrons can already be treated as quasiparticles. The cut-off of the quantum efficiency occurs when the maximum number of nonequilibrium QP in the slab reaches δN^*. The refined cut-off criteria $\delta N(\tau_{th}) = \delta N^*$ allows one to determine the efficiency of the quasiparticle multiplication

$$\zeta = \frac{N_0\,\Delta^2 w\,d\sqrt{\pi D\,\tau_{th}}\,(1 - I/I_C)}{h\nu} \qquad (4)$$

by substituting in the above equation the threshold values of the current or photon energy. The refined cut-off criteria and equation (4) show that the spectral cut-off can be rather observed in a dirty superconducting film that would have a small energy gap and a low density of electronic states. Assuming that the values of the current and wavelength defined by arrows in Figures 3 and 4 satisfy the cut-off criteria $\delta N = \delta N^*$, we calculated for each pair of the current and the wavelength the efficiency ζ and plotted it as function of the photon energy. The result is shown in Figure 6. An average efficiency of 0.1 suggests the absolute value of quantum yield $\approx$300 that corresponds to earlier measurements [13]. Thus the refinement eliminates contradictions of the hot-spot model with the already published experimental data.

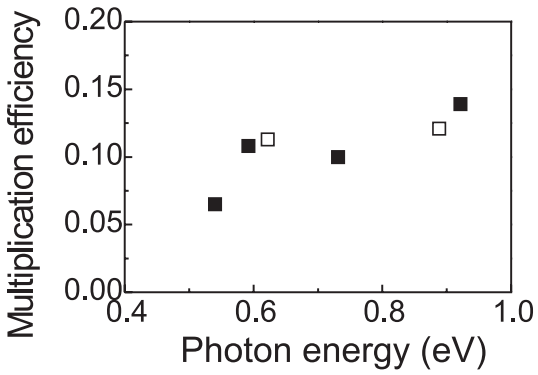

Fig. 6. Multiplication efficiency of quasiparticles for different photon energies concluded from current (open symbols) and spectral (closed symbols) dependence of the photon count rate.

The effectiveness of the QP multiplication increases with the photon energy. Although the physical reason for the increase is not quite clear, we speculate that it might be due to the splitting of the electron cascade into the electron and the phonon branches and to the energy loss associated with the phonon branch. The splitting occurs [7] around the Debye energy, which is slightly less than photon energies used in our experiment.

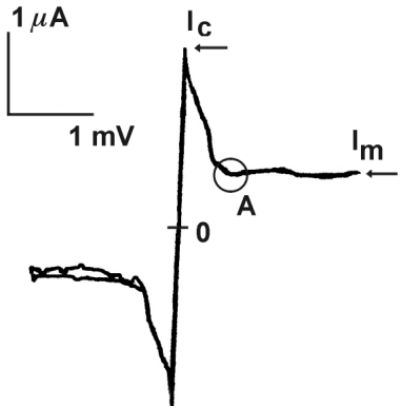

Fig. 7. Current-voltage characteristic of the NbN meander at 2 K. The critical current I_C and the current I_m equilibrating the walls of the normal domain are both marked by arrows. The area A marked by the circle corresponds to the smallest stable normal domain of a size approximately equal to the thermal healing length.

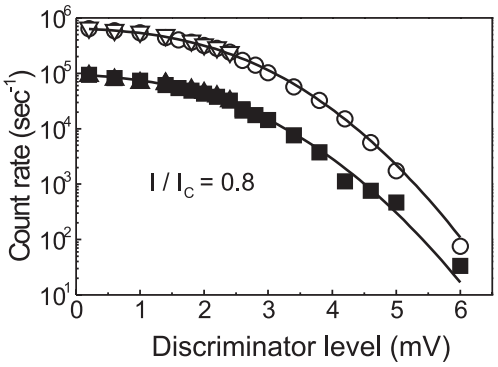

Fig. 8. The rate of dark (closed symbols) and photon (open symbols) counts at different discriminatory levels. Solid lines are the best fit assuming normal statistical distribution of the pulse amplitude.

4 Energy resolving capability

The normal conducting spot created in the meander by the joint action of a photon and the current relaxes via thermal phonons passing the excess energy to the substrate. Since the relaxation rate is fixed, the life-time of the resistive state increases with the full perturbation energy. Thus the duration of the voltage transient should depend on the energy of the photon that initiated the formation of the resistive state. In this section we show that the resistive state indeed memorizes the photon energy. Current-voltage curve of the meander recorded in the voltage-bias regime at 2 K is shown in Figure 7. After the critical value is reached, the current drops signaling formation of a normal domain. The area A corresponds to the smallest stable domain, which has a length of the order of the thermal healing length $L_T = (D\,\tau_E)^{1/2}$ where τ_E is the effective electron cooling time. When the voltage further increases, a plateau occurs at an almost constant current I_m that maintains the domain in equilibrium.

According to [16] the Stekly parameter, which measures the strength of the self-heating by the bias current, can be evaluated as $\alpha \approx (I_C/I_m)^2 = 25$. Using the resistivity of our specimen and the dc resistance ≈1.2 kΩ corresponding to the area A, we estimate a thermal healing length of ≈60 nm. Given the diffusivity of 3.5×10^{-5} m s^{-1}, such healing length suggests an effective electron cooling time of ≈100 ps. This value, being the upper limit for the electron-phonon interaction time, supports our estimate of the τ_{ep} in Section 2.1. Further using thus estimated electron cooling time, the measured critical current density 5.5×10^9 A m^{-2} and the electron specific heat at 2 K $c_E \approx 2\times10^2$ J m^{-3} K^{-1}, we calculated the value of the Stekly parameter $\alpha = \rho\, j_C^2\, \tau_E\, c_E^{-1}(T_C - T)^{-1}$ as it follows from the dynamic theory [16] of an electro-thermal domain and obtained $\alpha \approx 34$ in fair agreement with the value concluded from the I–V curve. The steady-state parameters deliver a self-consistent description of the electro-thermal domain in our specimen ensuring reliability of the following consideration.

The Stekly parameter $\alpha \gg 1$ suggests that even when $I \ll I_C$ self-heating strongly influences the dynamics of the normal domain. The critical energy that initiates the thermal roll-off or quenching in the current-biased meander can be presented [16] as

$$Q_0 = L_T\, w\, d\, c_E\, (T_C - T)\, \alpha\, i^2\ \ln\left(\frac{\alpha\, i^2}{\alpha\, i^2 - 2\,\theta}\right),$$
$$\text{with } \theta = \frac{T_C(I) - T}{T_C - T} \text{ and } i = \frac{I}{I_C}, \qquad (5)$$

where $T_C(I)$ denotes the temperature, which makes the critical current equal to the bias current I. Assuming the standard temperature dependence of the critical current, we find for our meander at $I/I_C = 0.8$ the critical energy $Q_0 = 0.51$ eV that is ≈3 times smaller than the energy of a 0.8–μm photon. Having in mind that the time constant of our bias scheme is larger than the electron-cooling time, we expect quenching to partly occur in our measurements. However, since the reciprocal bandpass of the readout electronics is even larger, the readout integrates the voltage transient delivering the signal whose amplitude preserves information on the photon energy.

Figure 8 shows the dark count rate and the photon count rate for 0.8–μm photons both measured with different discriminatory levels. When the level is set low all events are counted. Increase of the discriminatory level leaves more and more events unnoticed until at a higher level none of them is counted. Assuming the normal distribution of the pulse amplitude, we fit the integral of the distribution to the experimental data. Best-fit curves are shown in Figure 8. Two fitting parameters were used - the mean value and the dispersion of the normal distribution. We have found the best dispersion value 1.65 ± 0.03 mV for both dark and photon counts and the mean values 1.7 mV and 1.9 mV for dark and photon counts, respectively. In terms of the strength and statistical distribution, dark counts are identical to photon counts when photons have the critical energy Q_0. The wavelength of a photon having this critical energy is 2.4 μm that perfectly

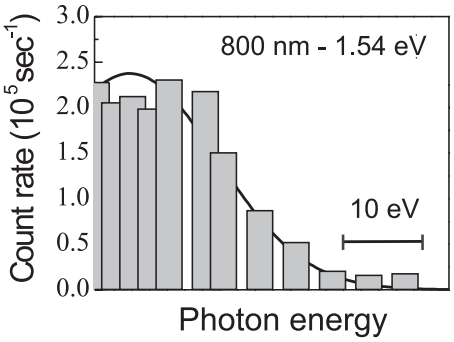

Fig. 9. Spectral histogram for 0.8–μm photons retrieved from the amplitude distribution of the photon and dark counts. Solid line shows a fitted Gaussian profile centered at 1.54 eV.

matches with the longest cut-off wavelength that we detected with our meanders. Relating the mean values of the pulse amplitudes to the energies of 0.8–μm and 2.4–μm photons we found a scaling factor of 0.14 mV/eV. Figure 9 presents the spectral histogram for 0.8–μm photons retrieved with this scaling factor from the experimental data. The best-fit envelope shown by the solid line represent a normal distribution with a dispersion of 6.5 eV. We will argue that the energy dissipated in the detector by the current limits the apparent energy resolution. After a photon has released an energy larger than Q_0, the normal domain starts to grow. The propagation velocity of the domain walls, i.e. the superconductor-normal interfaces, determines the grow rate of the normal domain. The velocity decreases as actual bias current drops following the domain growth. In our experiment the life-time of the domain roughly coincides with the time constant τ_B of the bias. The size of the domain, and consequently the energy dissipated by the bias, can be determined by integration of the Joule power with the particular current dependence of the interface velocity. Considering the simple step-edge heat-dissipation model, it can be shown [16] that the interface velocity $v = (\alpha\, D/\tau_E)^{1/2}(i - i_m)\,\theta^{-1/2}$ increases linearly with the current where $i_m = I_m/I_C$. With this dependence the expression for the Joule energy dissipated within the time τ_B takes the form

$$E_B = \frac{1}{5}\, I^2\, \rho\, \left(\frac{D}{\tau_E}\right)^{1/2}\, \frac{\tau_B^2}{w\, d}. \qquad (6)$$

Using $\tau_B = 0.5$ ns we found for our meanders a current contribution of ≈11 eV that is almost an order of magnitude larger than the energy of a 0.8–μm wavelength photon. Given the linear dependence of the response duration on the total energy released in the meander, the ratio of the mean amplitudes of photon and dark counts (see Fig. 8) correlates well with the energy contributed by the bias. Denoting by ϵ_1 and ϵ_2 the energies of 0.8–μm and 2.4–μm photon, respectively, we find $(E_B + \epsilon_1)/(E_B + \epsilon_2) \approx 1.09$ in agreement with the amplitude ratio 1.1 concluded from the experiment.

In summary, a reduced electron diffusivity and a reduced density of electronic states in our nanostructured disordered Nb(N) meanders allowed us to observe the cut-off of the quantum efficiency of the resistive state formation and to evaluate intrinsic effectiveness of the quasiparticle multiplication. The refined hot-spot model eliminated inconsistence with published so far experimental data. The life-time of the resistive state was shown to memorize the energy of the photon, which had initiated its formation. Although the present energy resolution was rather low, a proper optimization of the readout should reveal the ultimate energy resolving capability of the effect.

References

1. A. Semenov, G. Gol'tsman, A. Korneev, Physica C **351**, 349 (2001)
2. G.N. Gol'tsman, O. Okunev, G. Chulkova, A. Lipatov, A. Semenov, K. Smirnov, B. Voronov, C. Williams, R. Sobolevski, Appl. Phys. Lett. **79**, 705 (2001)
3. A. Verevkin, J. Zhang, R. Sobolewski, A. Lipatov, O. Okunev, G. Chulkova, A. Korneev, K. Smirnov, G. Gol'tsman, A. Semenov, Appl. Phys. Lett. **80**, 4687 (2002)
4. J. Zhang, W. Slysz, A. Pearlman, A. Verevkin, R. Sobolewski, O. Okunev, G. Chulkova, G.N. Gol'tsman, Phys. Rev. B **67**, 132508-1-4 (2003)
5. A. Semenov, A. Engel, K. Il'in, G. Gol'tsman, M. Siegel, H-W. Hübers, Eur. Phys. J. Appl. Phys. **21**, 171 (2003)
6. A. Semenov, A. Engel, K. Il'in, M. Siegel, H.-W. Hübers, IEEE Trans. Appl. Superconductivity **15**, 518 (2005); J. Kitaygorsky et al., IEEE Trans. Appl. Superconductivity **15**, 545 (2005)
7. A.G. Kozorezov, A.F. Volkov, J.K. Wigmore, A. Peacock, A. Poelaert, R. den Hartog, Phys. Rev. B **61**, 11807 (2000)
8. D. Prober, Appl. Phys. Lett. **62**, 2119 (1993)
9. H. Merkel, P. Khosropanah, D. Wilms Floet, P. Yagoubov, E. Kollberg, IEEE Transactions on Microwave Theory and Technique **48**, 600 (2000); T.M. Klapwijk, R. Barends, J.R. Gao, M. Hajenius, J.J.A. Baselmans, Proc. SPIE **5498**, 129 (2004)
10. L.N. Cooper, Phys. Rev. Lett. **6**, 689 (1961)
11. Direct measurements of the magnetic penetration length indicated normal conducting ≈0.4 nm thick layers at the film interfaces with the substrate and air and also ≈4 nm wide normal conducting areas along the strip edges. Together with the observed 15% non-homogeneity of the strip width this reduces the electrical cross-section of our meanders to ≈0.6 of the geometrical cross-section
12. J.-C. Villigier, B. Delaet, V. Larren, P. Febvre, J.W. Tao, G. Angenieux, Physica C **326**, 133 (1999)
13. K. Il'in, M. Lindgren, M. Currier, A. Semenov, G.N. Gol'tsman, R. Sobolewski, S. Cherednichenko, E. Gershenzon, Appl. Phys. Lett. **76**, 2752 (2000)
14. A. Anthore, H. Pothier, D. Esteve, Phys. Rev. Lett. **90**, 127001 (2003)
15. A. Semenov, A. Engel, H.-W. Hübers, K. Ilin, M. Siegel, in *Optical Sensing*, edited by B. Gulshaw, A. Mignani, R. Riesenberg, Proc. SPIE **5459**, 237 (SPIE, Bellingham, WA, 2004)
16. A.V. Gurevich, R.G. Mints, Rev. Modern Phys. **59**, 941 (1987)